Research Article | Vol. 27, No. 2 | 21 Jan 2019 | OPTICS EXPRESS 1310
Optics EXPRESS

Optimization of photonic nanojets generated by multilayer microcylinders with a genetic algorithm

YIN HUANG,[1,*] ZHISHEN ZHEN,[2] YUECHENG SHEN,[2,6] CHANGJUN MIN,[3] AND GEORGIOS VERONIS[4,5]

[1]*Department of Optoelectrics Information Science and Engineering, School of Physics and Electronics, Central South University, Changsha, Hunan 410012, China*
[2]*State Key Laboratory of Optoelectronic Materials and Technologies, School of Electronics and Information Technology, Sun Yat-Sen University, Guangzhou, Guangdong 510275, China*
[3]*Key Laboratory of Optoelectronic Devices and Systems of Ministry of Education and Guangdong Province, Shenzhen University, Shenzhen 518060, China*
[4]*School of Electrical Engineering and Computer Science, Louisiana State University, Baton Rouge, LA 70803, USA*
[5]*Center for Computation and Technology, Louisiana State University, Baton Rouge, LA 70803, USA*
[6]*yuechengshen@gmail.com*
[*]*yhuan15@csu.edu.cn*

Abstract: We employ a genetic algorithm coupled with Mie theory to optimize the magnetic field intensity profile of photonic nanojets (PNJs) generated by multilayer microcylinders at visible wavelengths in free space. We first optimize five-layer microcylinders to elongate the PNJs. We show that a properly designed five-layer microcylinder structure can generate an ultra-long PNJ with a beam length ~ 107.5 times the illumination wavelength λ_0. We then optimize five-layer microcylinders to narrow the waist of PNJs. We show that a PNJ with a full-width at half maximum waist of ~ $0.22\lambda_0$ can be obtained outside the surface of the optimized microcylinder. In addition, curved PNJs with subwavelength waist are also obtained. We finally optimize the five-layer structures for refractive index sensing based on the beam length of PNJs. The estimated minimum detectable refractive index variation when using this sensing method is ultra-small. Our results could potentially contribute to the development of a new generation of devices for optical nanoscopy and biophotonics, and greatly promote the practical applications of PNJs.

1. Introduction

The photonic nanojet (PNJ) is a non-resonant phenomenon [1,2]. A narrow and high-intensity optical field emerges on the shadow side of an illuminated microcylinder or microsphere, whose diameter is larger than the wavelength of the illuminating light [2,3]. This phenomenon can also be observed for three-dimensional particles of arbitrary shape with about one-wavelength diameter [4]. The physics and potential applications of PNJs were recently reviewed by Lukyanchuk *et al*. [5]. Over the past decade, many studies focused on extending the length of the nanojets to be as large as possible, since elongated PNJs can lead to applications in nanoparticle detection [2,6,7], optical data storage [8], and low-loss coupled-resonator optical waveguides [9]. Multilayer microspheres with graded refractive index exhibit elongated nanojets due to the suppression of the microspheres' backscattering [2,7]. In addition, graded-index dielectric particles can decrease the beam waist of nanojets [10]. Shen *et al*. proposed a two-layer microsphere structure consisting of a high refractive index shell and a low refractive index core. This refractive index distribution can make the power flow near the focal spot essentially parallel, and can thereby extend the beam length of the nanojet up to ~22 times the illumination wavelength

#349737 https://doi.org/10.1364/OE.27.001310
Journal © 2019 Received 2 Nov 2018; revised 15 Dec 2018; accepted 17 Dec 2018; published 15 Jan 2019

Optics EXPRESS

λ_0 [11]. Recently, a liquid-filled hollow microcylinder was designed to generate a nanojet with a decay length of over $100\lambda_0$ [12]. On the other hand, as narrow and high-intensity electromagnetic beams, PNJs can provide new pathways for high-resolution optical imaging [13, 14], ultrafast all-optical switching [15], and trapping of nanoparticles and cells [16]. Therefore, it is also highly desirable to explore a variety of designs to narrow the full width at half-maximum (FWHM) of PNJs. Wu *et al*. demonstrated that a nanojet with $0.485\lambda_0$ FWHM can be realized experimentally by decorating a microsphere surface with concentric rings [17]. By using a cylindrical metalens assembled by hexagonally arranged close-contact nanofibers, a nanojet with $0.244\lambda_0$ FWHM was attained theoretically by Yue *et al*. [18]. Similar resolution has been achieved by using the anomalously intensity-enhanced apodization effect [19]. Gu *et al*. demonstrated a narrow PNJ with FWHM of $0.287\lambda_0$ generated by overstepping the upper refractive index limit [20]. Most recently, Yang *et al*. reported a PNJ with FWHM as small as $0.25\lambda_0$ through a glass cuboid embedded in a dielectric cylinder [21].

All the studies mentioned above indicate that the shape and field distribution of PNJs are strongly dependent on the geometric parameters and material properties of the investigated microscatterers. The development of high-performance PNJ-based photonic devices, requires PNJs with improved beam length and FWHM. In order to further optimize the optical properties of PNJs, a natural solution would be to extend the design domain to incorporate more geometric and material parameters. However, the use of multi-parametric optimization for the design of PNJs has been very limited so far. In order to deal with large parameter spaces, genetic algorithms (GAs), which apply concepts of natural selection from evolutionary biology to intelligently search for optimum parameters [22], are ideal for this task. GAs have already been successfully used for the design of a variety of photonic structures and devices, such as optical couplers [23], slow-light waveguides [24], superscatterers [25], nanoparticle light concentrators [26], and optical metasurfaces [27].

In this paper, we employ a genetic algorithm coupled with Mie theory to optimize the PNJs generated by multilayer microcylinders at visible wavelengths in free space. We first optimize five-layer microcylinders to elongate PNJs. We show that a properly designed five-layer microcylinder structure can generate an ultra-long PNJ with a beam length ~107.5 times the illumination wavelength λ_0. The corresponding decay length is found to be $\sim 2000\lambda_0$. We then optimize the five-layer microcylinders to narrow the waist of PNJs. We show that a PNJ with a FWHM waist of $\sim 0.22\lambda_0$ is achieved outside the surface of the optimized microcylinder. In addition, curved PNJs, known as photonic hooks [4, 21, 28], with subwavelength waists are also obtained. We finally optimize the five-layer structure for refractive index sensing based on the beam length of PNJs. The estimated minimum detectable refractive index variation, when one uses this sensing method, is ultra-small. Although we focus here on two-dimensional infinitely long cylindrical structures, the proposed approach is quite general and could be also applied to three-dimensional spherical structures [29].

The remainder of the paper is organized as follows. In Section 2, we employ the full-wave Mie-Lorenz mode-expansion theory combined with the genetic algorithm to describe and analyze the scattering properties of the proposed five-layer cylindrical structure. Using this method, we optimize five-layer microcylinders for the generation of ultra-long PNJs, ultra-narrow PNJs, and for refractive index sensing in Subsections 3.1, 3.2, and 3.3, respectively. Finally, our conclusions are summarized in Section 4.

2. Theory

Our proposed five-layer cylindrical structure is normally illuminated by a TM plane wave propagating along the x direction with the magnetic field polarized along the cylinder (z) axis, as illustrated in Fig. 1. Taking advantage of the Mie-Lorenz mode-expansion method, which is based on multipolar expansion of the scattered field in terms of vector cylindrical wave

Optics EXPRESS

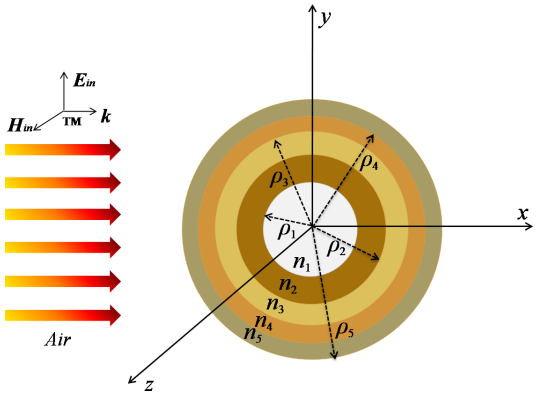

Fig. 1. Schematic of a five-layer core-shell cylindrical structure.

functions [30–32], the incident fields are given by

$$\mathbf{H}_{in} = \sum_{n=-\infty}^{\infty} H_n \mathbf{N}_n^{(1)}, \tag{1}$$

$$\mathbf{E}_{in} = \frac{ik_0}{\omega\epsilon_0} \sum_{n=-\infty}^{\infty} H_n \mathbf{M}_n^{(1)}, \tag{2}$$

with expansion coefficients $H_n = \frac{H_0(-i)^n}{k_0}$, where H_0 is the strength of the incident magnetic field, k_0 is the wave number in free space, and ϵ_0 is the dielectric permittivity of free space. $\mathbf{M}_n$ and $\mathbf{N}_n$ are vector cylindrical harmonics of the n-th order [30]. The superscript (1) indicates that for the vector cylindrical harmonics the radial dependence of the fields is given by Bessel functions of the first kind J_n. The fields in the core layer (Fig. 1) are given by

$$\mathbf{H}_1 = \sum_{n=-\infty}^{\infty} H_n [ic_n \mathbf{M}_n^{(1)} + d_n \mathbf{N}_n^{(1)}], \tag{3}$$

$$\mathbf{E}_1 = \frac{ik_1}{\omega\epsilon_1} \sum_{n=-\infty}^{\infty} H_n [ic_n \mathbf{N}_n^{(1)} + d_n \mathbf{M}_n^{(1)}], \tag{4}$$

where k_1 is the wave number in the core, and ϵ_1 is the dielectric constant of the material in the core. The fields in the shell with dielectric constant ϵ_m (Fig. 1) can be written as

$$\mathbf{H}_m = \sum_{n=-\infty}^{\infty} H_n [ig_{m,n} \mathbf{M}_n^{(1)} + f_{m,n} \mathbf{N}_n^{(1)} + ip_{m,n} \mathbf{M}_n^{(2)} + q_{m,n} \mathbf{N}_n^{(2)}], \tag{5}$$

$$\mathbf{E}_m = \frac{ik_m}{\omega\epsilon_m} \sum_{n=-\infty}^{\infty} H_n [ig_{m,n} \mathbf{N}_n^{(1)} + f_{m,n} \mathbf{M}_n^{(1)} + ip_{m,n} \mathbf{N}_n^{(2)} + q_{m,n} \mathbf{M}_n^{(2)}], \tag{6}$$

where k_m is the wave number in shell region m, where $m = 2, 3, 4, 5$. The superscript (2) indicates that for the vector cylindrical harmonics the radial dependence of the fields is given by Bessel functions of the second kind Y_n. The scattered fields outside the cylindrical structure are expressed as

$$\mathbf{H}_s = \sum_{n=-\infty}^{\infty} H_n [ib_n \mathbf{N}_n^{(3)} + a_n \mathbf{M}_n^{(3)}], \tag{7}$$

Optics EXPRESS

$$\mathbf{E}_s = \frac{ik_0}{\omega\epsilon_0}\sum_{n=-\infty}^{\infty} H_n[ib_n\mathbf{M}_n^{(3)} + a_n\mathbf{N}_n^{(3)}]. \tag{8}$$

The superscript (3) in the above equations indicates that for the vector cylindrical harmonics the radial dependence of the fields is given by Hankel functions of the first kind H_n. By enforcing the boundary conditions at each interface $\rho = \rho_j$, $j = 1, 2, 3, 4, 5$, we obtain the scattering coefficients a_n and b_n

$$a_n = 0, \tag{9}$$

$$b_n = \frac{U_n^{TM}}{U_n^{TM} + iV_n^{TM}}. \tag{10}$$

Note that the scattering coefficients a_n vanish when the direction of the incident light is normal to the cylinder axis z [30]. In Eq. (10) above, U_n^{TM} is given by

$$U_n^{TM} = \begin{vmatrix} M_1 & M_2 \\ M_3 & M_4 \end{vmatrix}, \tag{11}$$

where

$$M_1 = \begin{bmatrix} J_n(k_1\rho_1) & J_n(k_2\rho_1) & Y_n(k_2\rho_1) & 0 & 0 \\ \frac{J_n'(k_1\rho_1)}{\eta_1} & \frac{J_n'(k_2\rho_1)}{\eta_2} & \frac{Y_n'(k_2\rho_1)}{\eta_2} & 0 & 0 \\ 0 & J_n(k_2\rho_2) & Y_n(k_2\rho_2) & J_n(k_3\rho_2) & Y_n(k_3\rho_2) \\ 0 & \frac{J_n'(k_2\rho_2)}{\eta_2} & \frac{Y_n'(k_2\rho_2)}{\eta_2} & \frac{J_n'(k_3\rho_2)}{\eta_3} & \frac{Y_n'(k_3\rho_2)}{\eta_3} \\ 0 & 0 & 0 & J_n(k_3\rho_3) & Y_n(k_3\rho_3) \end{bmatrix},$$

$$M_2 = \begin{bmatrix} 0 & 0 & 0 & 0 & 0 \\ 0 & 0 & 0 & 0 & 0 \\ 0 & 0 & 0 & 0 & 0 \\ 0 & 0 & 0 & 0 & 0 \\ J_n(k_4\rho_4) & Y_n(k_4\rho_4) & 0 & 0 & 0 \end{bmatrix},$$

$$M_3 = \begin{bmatrix} 0 & 0 & 0 & \frac{J_n'(k_3\rho_3)}{\eta_3} & \frac{Y_n'(k_3\rho_3)}{\eta_3} \\ 0 & 0 & 0 & 0 & 0 \\ 0 & 0 & 0 & 0 & 0 \\ 0 & 0 & 0 & 0 & 0 \\ 0 & 0 & 0 & 0 & 0 \end{bmatrix},$$

$$M_4 = \begin{bmatrix} \frac{J_n'(k_4\rho_4)}{\eta_4} & \frac{Y_n'(k_4\rho_4)}{\eta_4} & 0 & 0 & 0 \\ J_n(k_4\rho_4) & Y_n(k_4\rho_4) & J_n(k_5\rho_5) & Y_n(k_5\rho_5) & 0 \\ \frac{J_n'(k_4\rho_4)}{\eta_4} & \frac{Y_n'(k_4\rho_4)}{\eta_4} & \frac{J_n'(k_5\rho_5)}{\eta_5} & \frac{Y_n'(k_5\rho_5)}{\eta_5} & 0 \\ 0 & 0 & J_n(k_5\rho_5) & Y_n(k_5\rho_5) & J_n(k_0\rho_5) \\ 0 & 0 & \frac{J_n'(k_5\rho_5)}{\eta_5} & \frac{Y_n'(k_5\rho_5)}{\eta_5} & \frac{J_n'(k_0\rho_5)}{\eta_0} \end{bmatrix},$$

and $\eta_j = \sqrt{\frac{\epsilon_j}{\mu_j}}$, $j = 0, 1, 2, 3, 4, 5$. All materials are non-magnetic, so that $\mu_j = \mu_0$, $j = 1, 2, 3, 4, 5$. In Eq. (10), V_n^{TM} is given by

$$V_n^{TM} = \begin{vmatrix} M_1^{\ddagger} & M_2^{\ddagger} \\ M_3^{\ddagger} & M_4^{\ddagger} \end{vmatrix}, \tag{12}$$

where $M_1^{\ddagger} = M_1$, $M_2^{\ddagger} = M_2$, $M_3^{\ddagger} = M_3$, and

$$M_4^{\ddagger} = \begin{bmatrix} \frac{J_n'(k_4\rho_4)}{\eta_4} & \frac{Y_n'(k_4\rho_4)}{\eta_4} & 0 & 0 & 0 \\ J_n(k_4\rho_4) & Y_n(k_4\rho_4) & J_n(k_5\rho_5) & Y_n(k_5\rho_5) & 0 \\ \frac{J_n'(k_4\rho_4)}{\eta_4} & \frac{Y_n'(k_4\rho_4)}{\eta_4} & \frac{J_n'(k_5\rho_5)}{\eta_5} & \frac{Y_n'(k_5\rho_5)}{\eta_5} & 0 \\ 0 & 0 & J_n(k_5\rho_5) & Y_n(k_5\rho_5) & Y_n(k_0\rho_5) \\ 0 & 0 & \frac{J_n'(k_5\rho_5)}{\eta_5} & \frac{Y_n'(k_5\rho_5)}{\eta_5} & \frac{Y_n'(k_0\rho_5)}{\eta_0} \end{bmatrix}.$$

Based on electromagnetic duality, the scattering coefficients b_n for a normally incident TE excitation are zero, while $a_n = \frac{U_n^{TE}}{U_n^{TE} + iV_n^{TE}}$, where U_n^{TE} and V_n^{TE} can be readily obtained by replacing ϵ with μ in Eqs. (11) and (12), respectively [30, 32].

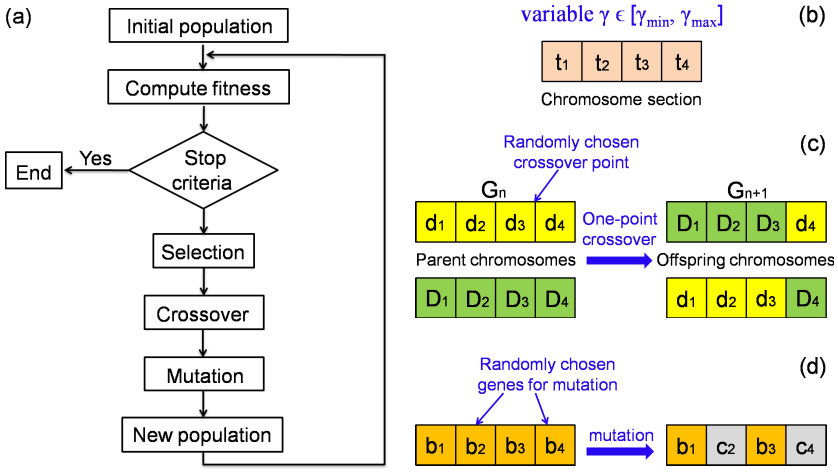

Fig. 2. (a) General flow of a genetic algorithm. (b) A coded chromosome section corresponding to a variable γ within a bounded range $[\gamma_{\min}, \gamma_{\max}]$. (c) Crossover process applied to a pair of chromosomes (d_1, d_2, d_3, d_4) and (D_1, D_2, D_3, D_4). Chromosomes of parents are split into two parts which are then exchanged to produce offspring with a randomly chosen crossover point. G_n and G_{n+1} represent generations n and $n + 1$, respectively. (d) Mutation process applied to a chromosome (b_1, b_2, b_3, b_4). Some genes of the chromosome change. The mutated genes are randomly chosen.

By using GAs, we seek to find both the radii $\{\rho_1, \rho_2, \rho_3, \rho_4\}$ and refractive indices $\{n_1, n_2, n_3, n_4, n_5\}$ at the wavelength of incident light $\lambda_0 = 632.8$ nm, corresponding to a He-Ne laser, to optimize the PNJs generated by our proposed five-layer microcylinders. The radius ρ_5 is fixed to be $5\lambda_0$ [11]. A flowchart of the GA used is shown in Fig. 2(a). The optimization process begins with the first generation of individuals (initial population), which are randomly generated. The number of individuals in each population is set to be 50 in our case. Large number of individuals can lead to high population diversity, and we can thus avoid convergence to local

Optics EXPRESS

maxima. The chromosome of each individual has 9 sections corresponding to the variables $\{\rho_1, \rho_2, \rho_3, \rho_4, n_1, n_2, n_3, n_4, n_5\}$ to be optimized. Each chromosome section consists of four genes [Fig. 2(b)]. Given a variable $\gamma \in \{\rho_1, \rho_2, \rho_3, \rho_4, n_1, n_2, n_3, n_4, n_5\}$ with lower and upper bounds $\gamma_{\min}$ and $\gamma_{\max}$, respectively, its coded chromosome section (t_1, t_2, t_3, t_4) corresponds to a real value of $\gamma = \gamma_{\min} + (\gamma_{\max} - \gamma_{\min}) * (t_1 \times 10^{-1} + t_2 \times 10^{-2} + t_3 \times 10^{-3} + t_4 \times 10^{-4})$, where t_i, $i = 1, 2, 3, 4$, is an integer in the range $0 \leq t_i \leq 9$. Next, the individuals are sorted based on their fitness, which is a measure of how close they are to our predefined optimization goal. In our case, the fitness is calculated through Mie theory. More specifically, Mie theory is used to calculate the magnetic field intensity distribution when the multilayer microcylinders are illuminated by a plane wave. The magnetic field intensity distribution is then used to calculate the fitness function used in the genetic algorithm, which is either the beam length or beam waist of the PNJs. When the structures are optimized for refractive index sensing, the fitness function is the variation in the beam length of the PNJs generated by the microcylinders that occurs for a variation in the refractive index of the core region divided by this refractive index variation. Individuals with relatively high fitness are more likely to be conserved based on the roulette wheel selection [33, 34], and combined together to form the reproduction pool. The GA randomly chooses pairs from the reproduction pool to act as parents. These parents are then crossed to breed offspring for the next generation. Figure 2(c) shows how crossover can be randomly executed using a one-point-crossover method. Both parent chromosomes are split into left and right sub-chromosomes at a randomly chosen crossover point, and each offspring obtains the left sub-chromosome of one parent and the right sub-chromosome of the other parent. To introduce extra variability into the population, mutation processes also occur at each generation based on the predefined probability of mutation. If a mutation occurs, the randomly chosen genes in the chromosome change [Fig. 2(d)]. To ensure the survival of the best individual in the current generation, this individual is cloned to enter the next generation. The overall optimization process is finally terminated when the stop criteria are met, that is, when the predefined maximum number of generations is reached. We choose the maximum number of generations to be 500.

3. Results

In this section, we use the Mie-Lorenz mode-expansion method coupled with the GA to optimize the PNJs generated by the five-layer cylindrical structures of Fig. 1 at the wavelength of $\lambda_0 = 632.8$ nm. The reported lowest available refractive index for natural optical materials in the visible light frequency range is ~1.377 [11,35]. Refractive indices from 1.4 to 2.0 can be obtained from various available glasses [36]. Higher refractive indices up to 3.4 can be achieved from various classes of materials such as semiconductors and oxides [37]. The refractive index of each layer in our structure n_i, $i = 1, 2, 3, 4, 5$, is therefore optimized within the range from 1.377 to 3.4. We use the commercial software COMSOL, which is based on the finite-element method, to numerically simulate the response of the proposed structures to a normally incident plane wave input.

3.1. Ultra-long photonic nanojets

We first optimize the five-layer microcylinder to maximize the length of the nanojet. To quantify the elongation of the PNJs, we define the PNJ beam length L as the distance on the x-axis from the cylinder's shadow-side surface to the point where the maximum PNJ intensity drops to twice the intensity of the incident light [6, 11]. By combining Mie theory and the GA with fitness function $F(\rho_1, \rho_2, \rho_3, \rho_4, n_1, n_2, n_3, n_4, n_5) = L(\rho_1, \rho_2, \rho_3, \rho_4, n_1, n_2, n_3, n_4, n_5)$, we find that for the optimized values of $\rho_1 = 2.05\lambda_0$, $\rho_2 = 2.92\lambda_0$, $\rho_3 = 4.90\lambda_0$, $\rho_4 = 4.98\lambda_0$, $n_1 = 1.47$, $n_2 = 1.55$, $n_3 = 2.85$, $n_4 = 1.55$, and $n_5 = 2.37$ the maximum beam length L is found to be $\sim 107.5\lambda_0$ at the wavelength of $\lambda_0 = 632.8$ nm. To the best of our knowledge, this is the longest PNJ generated by a microscatterer reported to date.

Optics EXPRESS

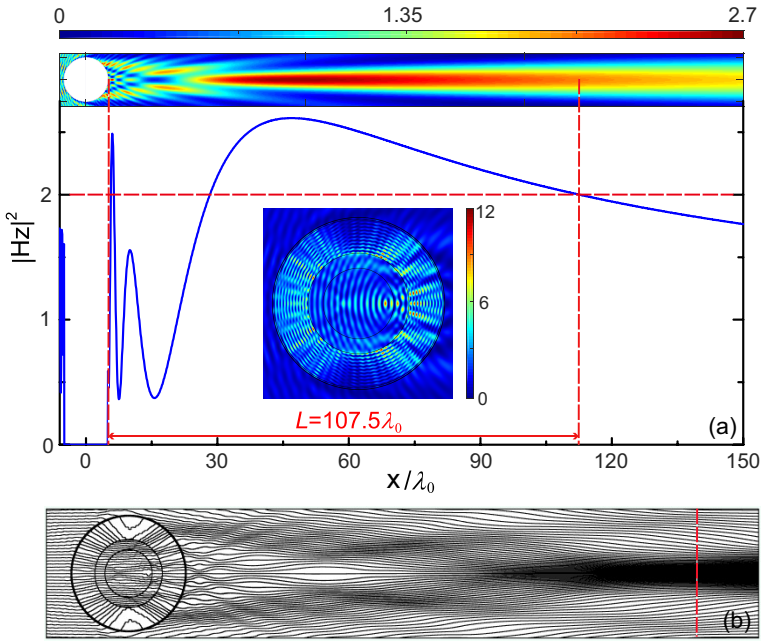

Fig. 3. (a) Magnetic field intensity profile and magnetic field intensity distribution along the x-axis at $y = 0$ for the optimized structure of Fig. 1 at the wavelength of $\lambda_0 = 632.8$ nm, when a plane wave with unit intensity is normally incident from the left. The inset shows the magnetic field intensity profile inside the microstructure. Results are shown for $\rho_1 = 2.05\lambda_0$, $\rho_2 = 2.92\lambda_0$, $\rho_3 = 4.90\lambda_0$, $\rho_4 = 4.98\lambda_0$, $\rho_5 = 5\lambda_0$, $n_1 = 1.47$, $n_2 = 1.55$, $n_3 = 2.85$, $n_4 = 1.55$, and $n_5 = 2.37$. The horizontal red dashed line corresponds to $|\mathrm{Hz}|^2 = 2$. The two vertical red dashed lines indicate the beam length of the optimized PNJ. (b) Streamlines of the Poynting vector for the optimized structure of Fig. 1 at the wavelength of $\lambda_0 = 632.8$ nm, when the plane wave is normally incident from the left. The vertical red dashed line corresponds to the focal plane of the optimized PNJ. All other parameters are as in Fig. 3(a).

The simulated magnetic field intensity profile outside the structure of Fig. 1 for the optimized parameters $n_1 = 1.47$, $n_2 = 1.55$, $n_3 = 2.85$, $n_4 = 1.55$, $n_5 = 2.37$, $\rho_1 = 2.05\lambda_0$, $\rho_2 = 2.92\lambda_0$, $\rho_3 = 4.90\lambda_0$, and $\rho_4 = 4.98\lambda_0$, when the plane wave with unit intensity is normally incident from the left, is shown in Fig. 3(a). The corresponding magnetic field intensity distribution along the x-axis at $y = 0$ is also shown in Fig. 3(a). We observe that the five-layer mircocylinder with the optimized parameters generates a significantly elongated PNJ ($L \sim 107.5\lambda_0$) in the x-direction at the wavelength of $\lambda_0 = 632.8$ nm. The simulated magnetic field intensity profile inside the microstructure is shown in the inset. Another quantity used to quantify the length of PNJs is the distance between the point of maximum PNJ light intensity to the point where the PNJ light intensity drops to $1/e$ times the maximum intensity [12, 21]. In our optimized structure, this distance is $\sim 2000\lambda_0$. We note that there is a trade-off between the length and waist of PNJs. Thus, the PNJ for our optimized structure has a relatively wide waist with $\sim 3.2\lambda_0$ FWHM. Figure 3(b) shows the streamlines of the Poynting vector for the optimized five-layer microcylinder. Similar to previously reported structures [11], we observe that the power flow inside the cylinder experiences alternating convergence and divergence. The divergence plays a role in slowing down the convergence. However, the divergence experienced inside our optimized five-layer microcylinder is greatly enhanced, and the overall alternating convergence and divergence process is further optimized. The power flow converges more smoothly outside the microcylinder and is more parallel near the focal spot. Thus, our optimized five-layer microcylinder results in an

Optics EXPRESS

ultra-long PNJ. We note that in the optimized structure the thickness of the fifth layer ($\rho_5 - \rho_4$) is only $0.02\lambda_0$, which is much smaller than the wavelength of light λ_0. However, we found that, if we remove this thin layer from the optimized structure of Fig.1, the beam length decreases significantly from $107.5\lambda_0$ to $86\lambda_0$ due to the relatively high refractive index of the fifth layer ($n_5 = 2.37$). In practice, the optimized structure can be realized using Pyrex glass, N-PSK3 glass, Cu_2O, and GaN. The refractive indices of Pyrex glass and N-PSK3 glass are 1.47 [38] and 1.55 [36], respectively, at the wavelength of $\lambda_0 = 632.8$ nm. Cu_2O and GaN have refractive indices very close to 2.85 [39, 40] and 2.37 [41], respectively, at the wavelength of $\lambda_0 = 632.8$ nm. Both Cu_2O [39, 40] and GaN [41] are lossless at this wavelength.

3.2. *Ultra-narrow photonic nanojets*

We next optimize the five-layer microcylinder to minimize the beam waist of PNJs. For large particles, the beam waist is equal to the FWHM of the magnetic field intensity distribution on the focal plane [5, 16, 21]. By defining the fitness function as $F(\rho_1, \rho_2, \rho_3, \rho_4, n_1, n_2, n_3, n_4, n_5) = FWHM(\rho_1, \rho_2, \rho_3, \rho_4, n_1, n_2, n_3, n_4, n_5)$, we find that for the optimized values of $\rho_1 = 1.29\lambda_0$, $\rho_2 = 3.96\lambda_0$, $\rho_3 = 4.57\lambda_0$, $\rho_4 = 4.80\lambda_0$, $n_1 = 3.17$, $n_2 = 1.60$, $n_3 = 1.86$, $n_4 = 1.62$, and $n_5 = 3.07$ the minimum beam waist can reach $\sim 0.22\lambda_0$ at the wavelength of $\lambda_0 = 632.8$ nm.

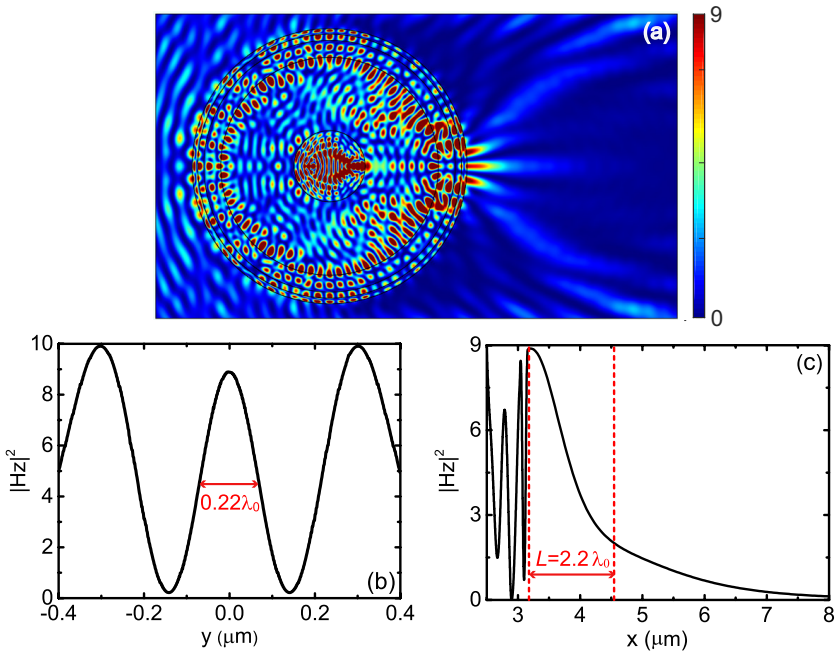

Fig. 4. (a) Magnetic field intensity profile for the optimized structure of Fig. 1 at the wavelength of $\lambda_0 = 632.8$ nm, when a plane wave with unit intensity is normally incident from the left. Results are shown for $n_1 = 3.17$, $n_2 = 1.60$, $n_3 = 1.86$, $n_4 = 1.62$, $n_5 = 3.07$, $\rho_1 = 1.29\lambda_0$, $\rho_2 = 3.96\lambda_0$, $\rho_3 = 4.57\lambda_0$, and $\rho_4 = 4.80\lambda_0$. (b) Magnetic field intensity distribution on the focal plane for the optimized structure of Fig. 1 at the wavelength of $\lambda_0 = 632.8$ nm, when a uniform plane wave is normally incident from the left. All other parameters are as in Fig. 4(a).(c) The magnetic field intensity distribution along the x-axis at $y = 0$ for the optimized structure of Fig. 1 at the wavelength of $\lambda_0 = 632.8$ nm, when a uniform plane wave with unit intensity is normally incident from the left. The two vertical red dashed lines indicate the beam length of the optimized PNJ. All other parameters are as in Fig. 4(a).

Optics EXPRESS

Figure 4(a) shows the simulated magnetic field intensity profile for the structure of Fig. 1 for the optimized parameters $n_1 = 3.17$, $n_2 = 1.60$, $n_3 = 1.86$, $n_4 = 1.62$, $n_5 = 3.07$, $\rho_1 = 1.29\lambda_0$, $\rho_2 = 3.96\lambda_0$, $\rho_3 = 4.57\lambda_0$, and $\rho_4 = 4.80\lambda_0$, when a plane wave with unit intensity is normally incident from the left. Interestingly, three nanojets outside the microcylinder can be observed. This phenomenon has also been observed in a cylinder with an embedded glass cuboid [21]. Figure 4(b) shows the FWHM beam waist for the optimized structure. We observe that the optimized five-layer microcylinder generates an ultra-narrow PNJ with FWHM of the magnetic field intensity distribution on the focal plane of $\sim 0.22\lambda_0$ at the wavelength of $\lambda_0 = 632.8$ nm. In comparison, we found that the corresponding FWHM of the optical intensity distribution is $\sim 0.30\lambda_0$. Figure 4(c) shows the magnetic field intensity distribution along the x-axis at $y = 0$ for the optimized structure. The focal spot is located outside the microcylinder and is very close to the surface boundary. The distance between the focal spot and the microcylinder surface boundary is ~ 20 nm. Compared to the ultra-long PNJ shown in Fig. 3(a), the beam length of the PNJ is shrunk from $\sim 107.5\lambda_0$ to $\sim 2.2\lambda_0$.

Figure 5 shows the streamlines of the Poynting vector for the optimized five-layer microcylinder shown in Fig. 4(a). For relatively large angles between the incident wave and the front surface of the cylinder, streams enter the core region and are split into three high-intensity substreams. The middle substreams then experience alternating divergence and convergence in the shell regions. After passing through the outermost layer with the high refractive index ($n_5 = 3.07$), the streams converge abruptly near the shadow surface of the microcylinder and form the ultra-narrow nanojet. Conventionally, the higher refractive index a single layer mircocylinder has, the narrower its FWHM waist is. However, the refractive index of the microcylinder has to be less than 2 to retain the nanojet outside the cylinder [2, 11, 12]. By introducing layers with low refractive indices ($n < 2$) between the outermost and innermost layers with high refractive indices ($n \geq 2$), the convergence process inside the optimized five-layer mircocylinder slows down. Thus, we not only achieve the reduction of the FWHM but we also prevent a focus spot from forming inside the microcylinder. For relatively small angles between the incident wave and the front surface of the cylinder, streams cannot enter the core region. They converge with the upper and bottom substreams from the core region leading to two high-intensity photonic hooks formed beside the ultra-narrow nanojet. The formation of the photonic nanojet and two photonic hooks could be regarded as an analogue of optical super-oscillation, where a super-narrow hot spot with high-power side lobes around it is formed [42,43]. The multilayer microcylinder with large radius is capable of supporting strong resonances with standing waves inside the cylinder [Fig. 4(a)]. Note that the strong resonances within the optimized microcylinder cannot be directly observed in the Poynting vector map because they are stationary along their propagation direction. In practice, to meet the requirements of the refractive indices for this optimized structure, $Al_xGa_{1-x}As$, F2 glass, SiN, N-SK16 glass, and ZnTe can be used. The refractive indices of F2 glass, SiN, and N-SK16 glass are 1.60 [36], 1.86 [44], and 1.62 [36], respectively, at the wavelength of $\lambda_0 = 632.8$ nm. SiN is lossless at this wavelength [44]. For $0.5 \leq x \leq 1$, the refractive index of $Al_xGa_{1-x}As$ changes from 3.5 to 3.1 with zero extinction coefficient at the wavelength of $\lambda_0 = 632.8$ nm [45]. ZnTe has refractive index very close to 3.07 at the wavelength of $\lambda_0 = 632.8$ nm, and is lossless at this wavelength as well [46].

Optics EXPRESS

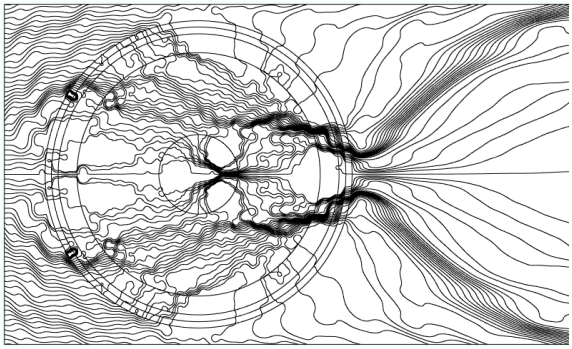

Fig. 5. Streamlines of the Poynting vector for the optimized structure of Fig. 1 at the wavelength of $\lambda_0 = 632.8$ nm, when a plane wave is normally incident from the left. All other parameters are as in Fig. 4(a).

3.3. Ultra-high sensitivity photonic nanojet-based refractive index sensing

It has been demonstrated both theoretically and experimentally that PNJs can be used for the detection of dielectric and metallic nanoparticles due to their highly focused light fields [2, 13, 16]. If a nanoparticle is inserted into the PNJ, the backscattering of the microcylinder can be perturbed. Most recently, Gu *et al*. showed theoretically that a single gold nanoparticle within a liquid-filled hollow-microcylinder can be detected [47] using PNJs. The contour lines of the PNJ for the liquid-filled hollow-microcylinder with a single gold nanoparticle are shifted compared to the case without a gold nanoparticle. In Subsections 3.1 and 3.2, we demonstrated that strong resonances can be induced inside the multilayer microcylinders. This feature provides an opportunity to boost light-matter interactions inside the cylinders, and thereby enables the detection of small refractive index changes inside the cylinders. In this subsection, the material in the core of our five-layer microcylinder structure is assumed to be a biologically compatible fluid, such as water. The refractive index of water is 1.333 [48, 49]. The fluid to be sensed flows over the core region. To characterize the sensing capability of the proposed five-layer microcylinder, we define the $figure\ of\ merit$ (FOM) as the variation in the beam length L of the PNJ generated by the five-layer microcylinder that occurs for a variation in the refractive index of the core region divided by this refractive index variation

$$FOM = \left|\frac{dL(n)}{dn}\right|, \tag{13}$$

where n is the refractive index of the fluid and L is the beam length of the PNJ. The beam length L is the only quantity that we measure for sensing. The variations in the beam length L are related to the refractive index variations Δn via $\Delta L = \frac{dL(n)}{dn}\Delta n$ [48, 49]. Denoting the smallest measurable change in beam length as $\Delta L_{\min}$, we obtain the following expression for the detection limit $\Delta n_{\min}$ of the five-layer microcylinder

$$|\Delta n_{\min}| = \left|\frac{\Delta L_{\min}}{FOM}\right|. \tag{14}$$

We note that the detection limit $|\Delta n_{\min}|$ decreases as the FOM increases.

We now optimize the five-layer microcylinder to maximize the FOM of the PNJ. The FOM in Eq. (13) can be calculated using the following finite-difference approximation $\frac{dL(n)}{dn} \simeq \frac{L(n+\Delta n)-L(n)}{\Delta n}$ [49]. This approximation improves in accuracy as $\Delta n \to 0$. In our calculations, we use $\Delta n = 10^{-4} << n_1$ [49]. By defining the fitness function as $F(\rho_1, \rho_2, \rho_3, \rho_4, n_2, n_3, n_4, n_5) =$

Optics EXPRESS

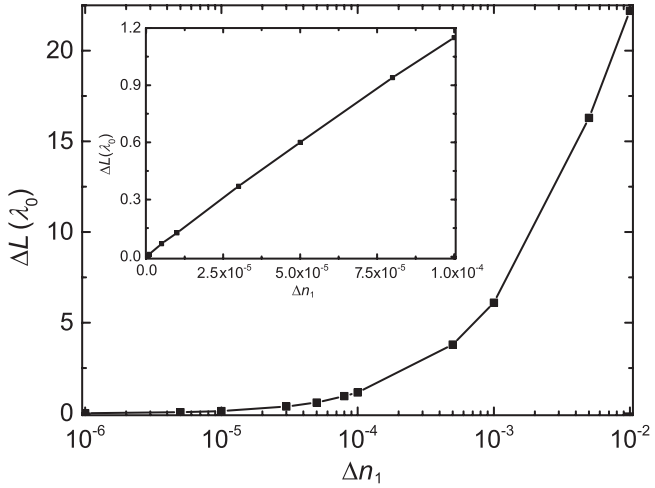

Fig. 6. Beam length variation ΔL for the optimized structure of Fig. 1 as a function of the refractive index variation in the core region Δn_1 at the wavelength of $\lambda_0 = 632.8$ nm, when the plane wave with unit intensity is normally incident from the left. The inset shows the beam length variation ΔL for the optimized structure of Fig. 1 for a variation in the refractive index of the core region n_1 from 1.333 to 1.3331 at the wavelength of $\lambda_0 = 632.8$ nm. Results are shown for $\rho_1 = 3.55\lambda_0$, $\rho_2 = 4.40\lambda_0$, $\rho_3 = 4.63\lambda_0$, $\rho_4 = 4.64\lambda_0$, $\rho_5 = 5\lambda_0$, $n_2 = 3.14$, $n_3 = 2.50$, $n_4 = 2.33$, and $n_5 = 1.86$.

$\left|L(\rho_1, \rho_2, \rho_3, \rho_4, n_2, n_3, n_4, n_5)|_{n_1=1.333+\Delta n} - L(\rho_1, \rho_2, \rho_3, \rho_4, n_2, n_3, n_4, n_5)|_{n_1=1.333}\right|$, we find that for the optimized values of $\rho_1 = 3.55\lambda_0$, $\rho_2 = 4.40\lambda_0$, $\rho_3 = 4.63\lambda_0$, $\rho_4 = 4.64\lambda_0$, $n_2 = 3.14$, $n_3 = 2.50$, $n_4 = 2.33$, and $n_5 = 1.86$ the variation in the beam length L for a refractive index variation of $\Delta n_1 = 10^{-4}$ in the core region can be as large as $\sim 1.15\lambda_0$ at the wavelength of $\lambda_0 = 632.8$ nm. The corresponding maximum FOM is $\sim 1.15 \times 10^4 \lambda_0$. The use of apertureless probes enables a potential of 1 nm to 10 nm optical near-field spatial resolution [50,51]. Therefore, assuming the smallest measurable change in the beam length $\Delta L_{\min}$ is 1 nm, the detection limit $\Delta n_{\min}$ can be as small as $\sim 1.37 \times 10^{-7}$.

Figure 6 shows the beam length variation ΔL for the optimized structure of Fig. 1 as a function of the refractive index variation in the core region Δn_1 at the wavelength of $\lambda_0 = 632.8$ nm, when a plane wave with unit intensity is normally incident from the left for $\rho_1 = 3.55\lambda_0$, $\rho_2 = 4.40\lambda_0$, $\rho_3 = 4.63\lambda_0$, $\rho_4 = 4.64\lambda_0$, $\rho_5 = 5\lambda_0$, $n_2 = 3.14$, $n_3 = 2.50$, $n_4 = 2.33$, and $n_5 = 1.86$. We observe that the beam length for such an optimized structure can experience a significant variation $\Delta L \sim 22.2\lambda_0$ for a refractive index variation in the core region Δn_1 of only 0.01. The inset in Fig. 6 also reveals that the variation in the beam length ΔL is approximately linearly dependent on the variation of the refractive index n_1,when n_1 varies between 1.333 and 1.3331.

Figure 7 shows the calculated magnetic field intensity profile associated with the optimized five-layer microcylinder of Fig. 1 for $\rho_1 = 3.55\lambda_0$, $\rho_2 = 4.40\lambda_0$, $\rho_3 = 4.63\lambda_0$, $\rho_4 = 4.64\lambda_0$, $\rho_5 = 5\lambda_0$, $n_1 = 1.333$, $n_2 = 3.14$, $n_3 = 2.50$, $n_4 = 2.33$, and $n_5 = 1.86$ at the wavelength of $\lambda_0 = 632.8$ nm, when a plane wave with unit intensity is normally incident from the left. Compared to the case of $n_1 = 1.333$, Figure 7 also shows the magnetic field intensity profile of the same optimized structure but with refractive index in the core region n_1 changed to be 1.343. We clearly observe a change in the magnetic field intensity profile outside the microcylinder when there is a refractive index change of 0.01 introduced in the core region. The magnetic field intensity distributions along the x-axis at $y = 0$ corresponding to the optimized five-layer microcylinder for $n_1 = 1.333$ (blue) and $n_1 = 1.343$ (green) are also shown in Fig. 7. For $n_1 = 1.333$, the

Optics EXPRESS

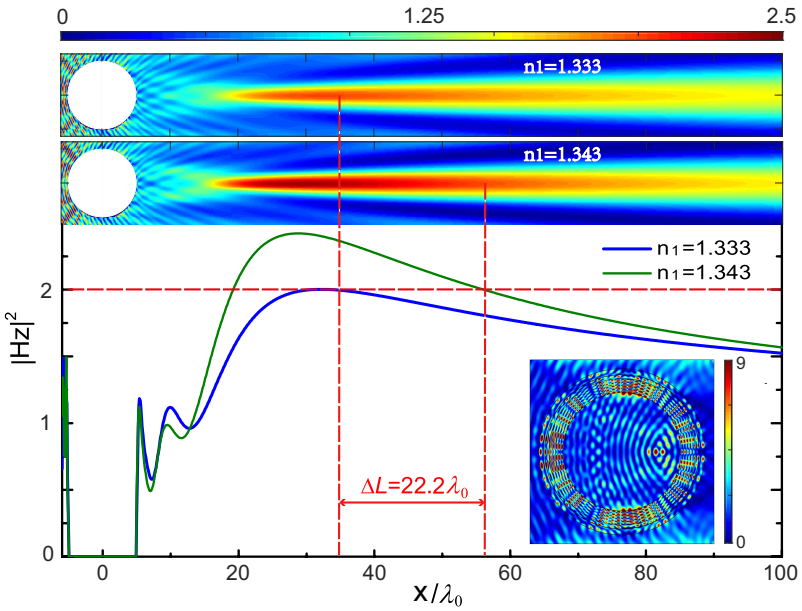

Fig. 7. Magnetic field intensity profiles for the optimized structure of Fig. 1 at the wavelength of $\lambda_0 = 632.8$ nm, when a plane wave with unit intensity is normally incident from the left. Results are shown for refractive index in the core region $n_1 = 1.333$ and $n_1 = 1.343$. Also shown are magnetic field intensity distributions along the x-axis at $y = 0$ for the optimized structure of Fig. 1 at the wavelength of $\lambda_0 = 632.8$ nm, when a plane wave with unit intensity is normally incident from the left, for refractive index in the core region $n_1 = 1.333$ (blue) and $n_1 = 1.343$ (green). The inset shows the magnetic field intensity profile inside the microstructure for refractive index in the core region $n_1 = 1.333$ at the wavelength of $\lambda_0 = 632.8$ nm. Results are shown for $\rho_1 = 3.55\lambda_0$, $\rho_2 = 4.40\lambda_0$, $\rho_3 = 4.63\lambda_0$, $\rho_4 = 4.64\lambda_0$, $\rho_5 = 5\lambda_0$, $n_2 = 3.14$, $n_3 = 2.50$, $n_4 = 2.33$, and $n_5 = 1.86$. The horizontal red dashed line corresponds to $|\mathrm{Hz}|^2 = 2$. The two vertical red dashed lines indicate the difference between the beam length for refractive index in the core region $n_1 = 1.333$ and $n_1 = 1.343$.

focal spot with normalized intensity of 2.01 is $\sim 27.2\lambda_0$ away from the shadow-side surface of the microcylinder. For $n_1 = 1.343$, the distance between the focal spot and the shadow-side surface of the microcylinder decreases slightly to $\sim 23.8\lambda_0$ but the normalized intensity of the focal spot increases to 2.42. Such an increase in the intensity of the focal spot leads to the beam length L greatly increasing from $\sim 28.9\lambda_0$ to $\sim 51.1\lambda_0$, that is, $\Delta L \sim 22.2\lambda_0$, when a refractive index variation of 0.01 is introduced in the core region. In addition, the simulated magnetic field intensity profile inside the structure for $n_1 = 1.333$ is shown in inset. We clearly observe strong resonances inside the microcylinder, which result in light being trapped in the structure for a longer duration [48]. This in turn leads to enhanced relative change in the maximum intensity, and thereby the change in the beam length induced by a small change in the refractive index of the core. We note that in the optimized structure the thickness of the fourth layer $(\rho_4 - \rho_3)$ is only $0.01\lambda_0$, which is much smaller than the wavelength of light λ_0. However, we found that, if we remove this thin layer from the optimized structure of Fig.1, the peak magnetic field intensity decreases significantly. For comparison, we also consider a single layer microcylinder with a radius of $5\lambda_0$ and a refractive index n. The beam length variation is only $0.2\lambda_0$ when the refractive index n is changed from 1.333 to 1.343.

Figures 8(a) and 8(b) show the streamlines of the Poynting vector for the optimized five-layer

Optics EXPRESS

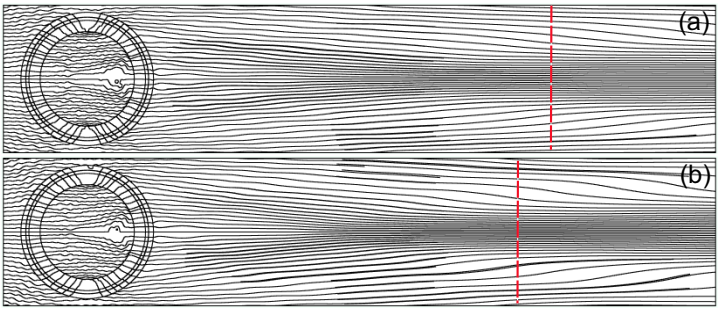

Fig. 8. (a) Streamlines of the Poynting vector for the optimized structure of Fig. 1 at the wavelength of $\lambda_0 = 632.8$ nm, when a plane wave is normally incident from the left for refractive index in the core region$n_1 = 1.333$. The vertical red dashed line indicates the focal plane of the PNJ. All other parameters are as in Fig. 6. (b) Same as in (a) except that $n_1 = 1.343$.

microcylinder shown in Fig. 7 with refractive index in the core region $n_1 = 1.333$ and $n_1 = 1.343$, respectively. Compared to the case of $n_1 = 1.333$, we observe that more power converges into the focal spot for $n_1 = 1.343$, which confirms that the increase in light intensity at the focal spot results from the change in the refractive index. Similarly to the case shown in Subsection 3.1 (Fig. 3), we observe the counterbalance between the convergence and divergence of power flow inside the cylinder. More specifically, the power flow diverges smoothly beyond the focal spot, which indicates that the light intensity decreases slowly along the x-axis from the focal point, as shown in Fig. 7. Thus, a relatively small change in the intensity at the focal point can produce a relatively large difference in the beam length. Experimentally, such an optimized microcylinder structure can be realized by using $Al_xGa_{1-x}As$, TiO_2 of anatase, ZnS, and SiN. As we mentioned in Subsection 3.2, SiN has refractive index of 1.86 and is lossless at the wavelength of $\lambda_0 = 632.8$ nm [44]. The refractive index of $Al_xGa_{1-x}As$ can be tuned to 3.14 for a certain value of x with zero extinction coefficient at the wavelength of $\lambda_0 = 632.8$ nm [45]. Moreover, the refractive indices of TiO_2 of anatase and ZnS are 2.5 [52] and 2.33 [53], respectively, and both of them are lossless at the wavelength of $\lambda_0 = 632.8$ nm. In addition, although interferometric optical sensors can provide detection limits on the order of 10^{-8} [49,54], their bulky size is not suitable for ultradense chip-scale integration. As an example, Berini investigated the sensing performance of a generic Mach-Zehnder interferometer (MZI) implemented with plasmonic waveguides. The reported detection limit can be as small as $\sim 1.5 \times 10^{-8}$ but with extremely long sensing length of 2039 μm [49]. In comparison, although the detection limit of our proposed nanojet-based sensor ($\sim 1.35 \times 10^{-7}$) is ~9.1 times larger than that of the MZI structure ($\sim 1.5 \times 10^{-8}$), the diameter of our multilayer microcylinder ($2R = 10\lambda_0 = 6.328$ μm) is ~322.2 times smaller than the sensing length of the MZI structure (2039 μm) [49].

4. Conclusions

In this paper, we designed microscale five-layer cylindrical structures to optimize their photonic nanojets at the wavelength of λ_0 =632.8 nm. We used the Mie-Lorenz mode-expansion theory combined with a genetic algorithm in order to choose the geometric and material parameters of the five-layer microcylinders so as to achieve the optimization of the magnetic field intensity profile of the PNJs. We first optimized the five-layer microcylinders to maximize the length of PNJs. We found that a properly designed five-layer microcylinder structure can generate an ultra-long PNJ with a beam length of ~ 107.5 λ_0 and a decaying length of $\sim 2000\lambda_0$. Such large length is achieved due to the optimized counterbalance between the convergence and divergence

Optics EXPRESS

inside the five-layer microcylinder. We then optimized the five-layer microcylinders to narrow the waists of PNJs. We found that a PNJ with a FWHM waist of $\sim 0.22\lambda_0$ can be achieved in the near-field zone. We not only reduced the FWHM using high-index layers in the outermost and innermost layers, but also prevented the focus spot from forming inside the microcylinder by using low-index layers between the outermost and innermost layers. In addition, curved PNJs, known as photonic hooks, with subwavelength waists were also obtained. The coupling between the power flows and the standing waves supported by the optimized five-layer microcylinder played an important role in maintaining the strong focus for the generated PNJs. We finally optimized the five-layer structure for refractive index sensing based on the beam length of the PNJ. The estimated minimum detectable refractive index variation based on this sensing method is ultra-small. Such an ultra-high sensitivity is attributed to the strong resonances inside the optimized microcylinder, and the parallel power flow with small divergence angle near the focal spot. The strong resonances can lead to a relatively large change in the intensity at the focal spot induced by a small refractive index change in the core region of the optimized microcylinder. The parallel power flow with small divergence angle near the focal spot can lead to a relatively large change in the beam length of PNJ, induced by a relatively small change in the intensity at the focal spot. We also confirmed these findings with full-wave finite-element simulations.

As final remarks, we note that the multilayer microcylinder structures can be fabricated by combining chemical vapor deposition with atomic layer deposition [55,56]. Additional processes of etching and annealing followed by chemical vapor deposition and atomic layer deposition are required to fabricate the hollow multilayer microcylinder structures [56]. Although we focused here on five-layer cylinders, the proposed approach can be applied to cylinders with any number of layers. However, we found that increasing the number of layers beyond five leads to insignificant improvement of the structure's performance. The mode-expansion method coupled with a GA could also be applied to optimize photonic nanojet properties of multilayer microspheres and other microparticles. Our results could be potentially important for the development of a new generation of devices for nanometrology, chip-scale biosensing, imaging nano-objects, and greatly promote the practical applications of PNJs.

Funding

National Natural Science Foundation of China (NSFC) (61605252, 91750205); Hunan Provincial Natural Science Foundation of China (2017JJ3375); National Key Research and Development Program of China (2016YFC0102401); National Science Foundation (NSF) (1254934).

References

1. D. Benincasa, P. Barber, J. Zhang, W. Hsieh, and R. Chang, "Spatial distribution of the internal and near-field intensities of large cylindrical and spherical scatterers," Appl. Opt. **26**, 1348–1356 (1987).
2. Z. Chen, A. Taflove, and V. Backman, "Photonic nanojet enhancement of backscattering of light by nanoparticles: a potential novel visible-light ultramicroscopy technique," Opt. Express **12**, 1214–1220 (2004).
3. N. Horiuchi, "Photonic nanojets," Nat. Photonics **6**, 138–139 (2012).
4. I. Minin and O. Minin, *Diffractive Optics and Nanophotonics* (Springer, 2016).
5. B. Lukyanchuk, R. Dominguez, I. Minin, O. Minin, and Z. Wang, "Refractive index less than two: photonic nanojets yesterday, today and tomorrow," Opt. Mater. Express **7**, 1820–1847 (2017).
6. S. Kong, A. Taflove, and V. Backman, "Quasi one-dimensional light beam generated by a graded-index microsphere," Opt. Express **17**, 3722–3731 (2009).
7. C. Ruiz and J. Simpson, "Detection of embedded ultrasubwavelength-thin dielectric features using elongated photonic nanojets," Opt. Express **18**, 16805–16812 (2010).
8. S. Kong, A. Sahakian, A. Taflove, and V. Backman, "Photonic nanojet-enabled optical data storage," Opt. Express **16**, 13713–13719 (2008).
9. S. Yang and V. Astratov, "Photonic nanojet-induced modes in chains of size-disordered microspheres with an attenuation of only 0.08 dB per sphere," Appl. Phys. Lett. **92**, 261111 (2008).
10. C. Liu, T. Yen, O. Minin, and I. Minin, "Engineering photonic nanojet by a graded-index micro-cuboid," Phys. E **98**, 105–110 (2018).

Optics EXPRESS

11. Y. Shen, L. Wang, and J. Shen, "Ultralong photonic nanojet formed by a two-layer dielectric microsphere," Opt. Lett. **39**, 4120–4123 (2014).
12. G. Gu, R. Zhou, Z. Chen, H. Xu, G. Cai, Z. Cai, and M. Hong, "Super-long photonic nanojet generated from liquid-filled hollow microcylinder," Opt. Lett. **40**, 625–628 (2015).
13. H. Yang, R. Trouillon, G. Huszka, and M. Gijs, "Super-resolution imaging of a dielectric microsphere is governed by the waist of its photonic nanojet," Nano Lett. **16**, 4862–4870 (2016).
14. Z. Wang, W. Guo, L. Li, B. Lukyanchuk, A. Khan, Z. Liu, Z. Chen, and M. Hong, "Optical virtual imaging at 50 nm lateral resolution with a white-light nanoscope," Nat. Commun. **2**, 218 (2011).
15. B. Born, J. Krupa, S. Gagnon, and J. Holzman, "Integration of photonic nanojets and semiconductor nanoparticles for enhanced all-optical switching," Nat. Commun. **6**, 8097 (2015).
16. Y. Li, H. Xin, X. Liu, Y. Zhang, H. Lei, and B. Li, "Trapping and detection of nanoparticles and cells using a parallel photonic nanojet array," ACS Nano **10**, 5800–5808 (2016).
17. M. Wu, B. Huang, R. Chen, Y. Yang, J. Wu, R. Ji, X. Chen, and M. Hong, "Modulation of photonic nanojets generated by microspheres decorated with concentric rings," Opt. Express **25**, 20096–20103 (2015).
18. L. Yue, B. Yan, and Z. Wang, "Photonic nanojet of cylindrical metalens assembled by hexagonally arranged nanofibers for breaking the diffraction limit," Opt. Lett. **41**, 1336–1339 (2016).
19. L. Yue, B. Yan, J. Monks, R. Dhama, Z. Wang, O. Minin, and I. Minin, "Intensity-enhanced apodization effect on an axially illuminated circular-column particle-lens," Ann. Phys. **530**, 1700384 (2018).
20. G. Gu, J. Song, H. Liang, M. Zhao, Y. Chen, and J. Qu, "Overstepping the upper refractive index limit to form ultra-narrow photonic nanojets," Sci. Reports **7**, 5635 (2017).
21. J. Yang, P. Twardowski, P. Gerard, Y. Duo, J. Fontaine, and S. Lecler, "Ultra-narrow photonic nanojets through a glass cuboid embedded in a dielectric cylinder," Opt. Express **26**, 3723–3731 (2018).
22. D. Goldberg, *Genetic Algorithms in Search, Optimization, and Machine Learning,* (Addison Wesley, 1989).
23. Y. Huang, C. Min, and G. Veronis, "Compact slit-based couplers for metal-dielectric-metal plasmonic waveguides," Opt. Express **25**, 22233–22244 (2012).
24. T. Pickering, J. Hamm, A. Page, S. Wuestner, and O. Hess, "Cavity-free plasmonic nanolasing enabled by dispersionless stopped light," Nat. Commun. **5**, 4972 (2014).
25. A. Mirzaei, A. Miroshnichenko, I. Shadrivov, and Y. Kivshar, "Superscattering of light optimized by a genetic algorithm," Appl. Phys. Lett. **105**, 011109 (2014).
26. C. Forestiere, A. Pasquale, A. Capretti, G. Miano, A. Tamburrino, S. Lee, B. einhard, and L. Negro, "Genetically engineered plasmonic nanoarrays," Nano Lett. **12**, 2037–2044 (2012).
27. S. Zanjani, S. Inampudi, and H. Mosallaei, "Adaptive genetic algorithm for optical metasurfaces design," Sci. Reports **8**, 11040 (2018).
28. L. Yue, O. Minin, Z. Wang, J. Monks, A. Shalin, and I. Minin, "Photonic hook: a new curved light beam," Opt. Lett. **43**, 771–774 (2018).
29. Y. Geints, A. Zemlyanov, O. Minin, and I. Minin, "Systematic study and comparison of photonic nanojets produced by dielectric microparticles in 2D- and 3D-spatial configurations," J. Opt. **20**, 065606 (2018).
30. C. Bohren and D. Huffman, *Absorption and Scattering of Light by Small Particles* (Wiley, 1998).
31. Y. Huang, Y. Shen, C. Min, and G. Veronis, "Switching photonic nanostructures between cloaking and superscattering regimes using phase-change materials," Opt. Mater. Express **8**, 1672–1685 (2018).
32. P. Chen, J, Soric, and A. Alu, "Invisibility and cloaking based on scattering cancellation," Adv. Mater. **24**, OP281–OP304 (2012).
33. D. Simon, *Evolutionary Optimization Algorithms* (Wiley, 2013).
34. M. Melanie, *An Introduction to Genetic Algorithms* (MIT, 1996).
35. E. Schubert, J. Kim, and J. Xi, "Low-refractive-index materials: A new class of optical thin-film materials," Phys. Status Solldi (b) **244**, 3002–3008 (2007).
36. O. Mazurin, M. Streltsina, and T. Shavaikovskaya, *Handbook of Glass Data* (Elsevier, 1993).
37. R. Reddy, K. Gopal, K. Narasimhulu, L. Reddy, K. Kumar, G. Balakrishnaiah, and M. Kumar, "Interrelationship between structural, optical, electronic and elastic properties of materials," J. Alloy. Compd. **473**, 28–35 (2009).
38. P. Tobiska, O. Hugon, A. Trouillet, and H. Gagnaire, "An integrated optic hydrogen sensor based on SPR on palladium," Sensors Actuators B: Chem. **74**, 168–172 (2001).
39. D. Tahir and S. Tougaard, "Electronic and optical properties of Cu, CuO and Cu_2O studied by electron spectroscopy," J. Physics: Condens. Matter **24**, 175002 (2012).
40. A. Rakhshani and J. Varghese, "Optical absorption coefficient and thickness measurement of electrodeposited films of Cu_2O," Phys. Status Solidi (a) **101**, 479–486 (1987).
41. R. Goldhahn, J. Scheiner, S. Shokhovets, T. Frey, U. Koler, D. As, and K. Lischka, "Refractive index and gap energy of cubic $In_xGa_{1-x}N$," Appl. Phys. Lett. **76**, 291–293 (2000).
42. R. Remez and A. Arie, "Super-narrow frequency conversion," Optica **2**, 472–475 (2015).
43. Y. Ogura, M. Aino, and J. Tanida, "Design and demonstration of fan-out elements generating an array of subdiffraction spots," Opt. Express **22**, 25196–25207 (2014).
44. H. Nagel, A. Aberle, and R. Hezel, "Optimised antireflection coatings for planar silicon solar cells using remote PECVD silicon nitride and porous silicon dioxide," Prog. Photovoltaics Res. Appl. **7**, 245–260 (1999).
45. D. Aspnes, S. Kelso, R. Logan, and R. Bhat, "Optical properties of $Al_xGa_{1-x}As$," J. Appl. Phys. **60**, 754–767

Optics EXPRESS

(1986).
46. K. Sato and S. Adachi, "Optical properties of ZnTe," J. Appl. Phys. **73**, 926–931 (1993).
47. G. Gu, J. Song, M. Chen, X. Peng, H. Liang, and J. Qu, "Single nanoparticle detection using a photonic nanojet," Nanoscale **10**, 14182–14189 (2018).
48. Y. Huang, C. Min, P. Dastmalchi, and G. Veronis, "Slow-light enhanced subwavelength plasmonic waveguide refractive index sensors," Opt. Express **23**, 14922–14936 (2015).
49. P. Berini, "Bulk and surface sensitivities of surface plasmon waveguides," New J. Phys. **10**, 105010 (2008).
50. F. Zenhausern, Y. Martin, and H. Wickramasinghe, "Scanning interferometric apertureless microscopy: optical imaging at 10 angstrom resolution," Science **269**, 1083–1085 (1995).
51. R. Hillenbrand and F. Keilmann, "Material-specific mapping of metal/semiconductor/dielectric nanosystems at 10 nm resolution by backscattering near-field optical microscopy," Appl. Phys. Lett. **80**, 25–27 (2002).
52. S. Tanemura, L. Miao, P. Jin, K. Kaneko, A. Terai, and N. Gabain, "Optical properties of polycrystalline and epitaxial anatase and rutile TiO_2 thin films by rf magnetron sputtering," Appl. Surf. Sci. **212**, 654–660 (2003).
53. S. Ozaki and S. Adachi, "Optical constants of cubic ZnS," Jpn. J. Appl. Phys. **32**, 5008–5013 (1993).
54. X. Fan, I. White, S. Shopova, H. Zhu, J. Suter, and Y. Sun, "Sensitive optical biosensors for unlabeled targets: a review," Anal. Chimica Acta **620**, 8–26 (2008).
55. L. Zhang, R. Tu, and H. Dai, "Parallel core-shell metal-dielectric-semiconductor germanium nanowires for high-current surround-gate field-effect transistors," Nano Lett. **6**, 2785–2789 (2006).
56. C. Guan, X. Wang, Q. Zhang, Z. Fan, H. Zhang, and H. Fan, "Highly stable and reversible lithium storage in SnO_2 nanowires surface coated with a uniform hollow shell by atomic layer deposition," Nano Lett. **14**, 4852–4858 (2014).